

VinePT-Map: Pole-Trunk Semantic Mapping for Resilient Autonomous Robotics in Vineyards

Giorgio Audrito^{1,2}, Mauro Martini^{1,3}, Alessandro Navone^{1,3}, Giorgia Galluzzo¹ and Marcello Chiaberge^{1,3}

Abstract—Reliable long-term deployment of autonomous robots in agricultural environments remains challenging due to perceptual aliasing, seasonal variability, and the dynamic nature of crop canopies. Vineyards, characterized by repetitive row structures and significant visual changes across phenological stages, represent a pivotal field challenge, limiting the robustness of conventional feature-based localization and mapping approaches. This paper introduces VinePT-Map, a semantic mapping framework that leverages vine trunks and support poles as persistent structural landmarks to enable season-agnostic and resilient robot localization. The proposed method formulates the mapping problem as a factor graph, integrating GPS, IMU, and RGB-D observations through robust geometrical constraints that exploit vineyard structure. An efficient perception pipeline based on instance segmentation and tracking, combined with a clustering filter for outlier rejection and pose refinement, enables accurate landmark detection using low-cost sensors and onboard computation. To validate the pipeline, we present a multi-season dataset for trunk and pole segmentation and tracking. Extensive field experiments conducted across diverse seasons demonstrate the robustness and accuracy of the proposed approach, highlighting its suitability for long-term autonomous operation in agricultural environments.

I. INTRODUCTION

The deployment of autonomous robotic systems in agriculture represents a pivotal step toward addressing global labor shortages and increasing operational efficiency [1]. Although considerable progress has been made in recent years [2], [3], achieving a reliable and persistent deployment in real-world agricultural contexts remains a formidable challenge. Most prior work has concentrated on row-based crops [4], and has tackled challenges including localization [5], [6], path planning [7], navigation [8], harvesting [9], [10], and vegetation assessment [11]. The dynamic, visually repetitive, and constantly changing nature of agricultural environments poses significant challenges to perception, localization, and mapping, making robot deployment far from straightforward [12] [13].

Vineyards exemplify these complexities. Their highly repetitive row geometry gives rise to perceptual aliasing [14], while fluctuations in canopy density, illumination conditions, and phenological stages significantly transform the environment’s visual characteristics over time [15]. Therefore, mapping and localization strategies that depend on generic

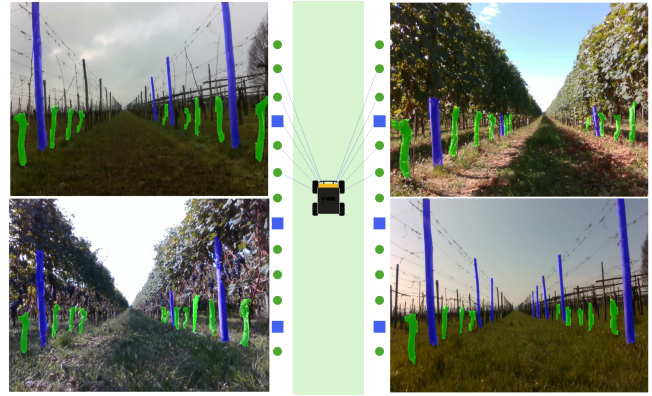


Fig. 1. VinePT-Map enables robotic platforms to build permanent landmarks map in vineyards for robust autonomous operation in all the seasons.

visual features are inevitably susceptible to robustness issues, which restricts their suitability for sustained, long-term deployment. As a result, the applicability of canopy-centric localization and mapping methodologies is limited to short-term data acquisition campaigns and cannot generalize to extended time horizons and to diverse environmental conditions [16] [17]. Recent advances in mobile robotics have underscored the advantages of incorporating structural or semantic landmarks for navigation [18] [19]. This work focuses on the idea of a semantic mapping framework for vineyards based on persistent landmarks, specifically vine trunks and support poles. These structural elements of the field provide a robust and season-agnostic spatial foundation for accurate localization and mapping of autonomous robots. The proposed approach mirrors fundamental principles of human spatial cognition: humans navigate complex environments by forming cognitive maps anchored to stable, semantically meaningful landmarks, rather than relying on superficial visual appearances that may vary [20]. Similarly, rather than relying on the variable visual cues of foliage or grass, which undergo seasonal changes, this work relies on the vineyard’s permanent skeletal infrastructure.

We propose VinePT-Map: a poles-trunks semantic mapping framework based on factor graphs. This graphical representation allows for the seamless fusion of GPS-RTK and RGB-D data, posing geometrical constraints to exploit the structure of the field. By decoupling variables and measurements, the approach naturally supports incremental refinement of object poses and map consistency, while maintaining robustness to sensor noise and partial observations. The perception entails an instance segmentation and

This work was supported by the PoliTO Interdepartmental Centre for Service Robotics (PIC4SeR).

¹Department of Electronics and Telecommunications, Politecnico di Torino, 10129, Torino, Italy.

² giorgio.audrito@polito.it

³ {name}.{surname}@polito.it

tracking stage, a precise reference point computation for map projection, and a landmark data association step for robust outlier rejection. The overall system can be deployed directly on the robot with low-power consumption and low-cost hardware, building the map of the field at runtime. An extensive validation has been performed to test the perception and mapping algorithms across all the seasons in a real vineyard, as seen in Fig. 1. We validate the visual perception with a new custom dataset for instance segmentation and tracking of poles and trunks, while the mapping results have been quantitatively computed using georeferenced positions of the landmarks. The implementation and the access to data will be publicly released in the VinePT-Map repository ¹.

The contributions of the paper can be summarized as:

- VinePT-Map: a poles-trunks semantic mapping methodology based on factor graphs to map permanent structural elements, reducing map complexity and increasing resilience to environmental aliasing using consumer-grade RGB-D cameras;
- A dataset to train and test instance segmentation and tracking of poles and trunks, spanning from February to September;
- An efficient segmentation and tracking pipeline for poles and trunks, coupled with a clustering filter to reject outliers, that can incrementally create a map while the robot navigates through the field over the entire year;
- A thorough experimental evaluation on the field of both perception and mapping performance across seasons and varying vineyard conditions, and an ablation study highlighting the impact of perceptual methods on mapping performance.

II. RELATED WORKS

Autonomous navigation in precision viticulture faces critical challenges from perceptual aliasing and seasonal morphological volatility, thus making traditional geometric mapping inadequate [14] [18]. State-of-the-art research is shifting towards the integration of semantic-aware Simultaneous Localization and Mapping (SLAM) systems, with the objective of leveraging semantic landmarks to effectively address the geometric ambiguities inherent in repetitive crop rows [18] [21]. This paradigm relies heavily on edge-deployed deep learning architectures, such as YOLO [22], to achieve real-time feature extraction in unstructured environments. In order to exceed the constraints imposed by purely visual systems, these semantic detections are combined with 3D LiDAR data [23]. Recently proposed SLAM frameworks capitalize on these detections to model agricultural environments robustly [24]. For instance, VineSLAM [19] employs semi-plane segmentation to map parallel rows, while Tree-SLAM [21] treats individual trunks as discrete entities within factor graphs. Furthermore, the introduction of "semantic walls" has been shown to act as a pseudo-rigid constraint within semantic particle filters, leading to a significant reduction in longitudinal drift along symmetrical corridors [19]. In order

to ensure temporal invariance and enable year-round operation despite drastic canopy variations, recent approaches employ topological neighborhood descriptors and multi-metric tracking frameworks for robust data association [21] [25]. In view of the current state of the art, we posit that leveraging permanent semantic features, such as poles and trunks, rather than raw geometric data, provides the requisite precision for complex, long-term autonomous operation.

III. METHODOLOGY

This section presents the pipeline for building a georeferenced, semantically annotated map of the structural elements of vineyards. The proposed pipeline transforms raw RGB-D images, IMU and GPS measurements into a globally consistent set of landmark positions, each annotated with a semantic class label and an associated uncertainty estimate.

A. Methodology overview

The system is organized into a two cascaded stages reported in Fig.2. The first stage, the *perception front-end*, operates on each RGB-D frame pair to segment, and track vineyard vine trunks and support poles in order to estimate their positions in camera reference frame. The second stage, the *mapping back-end*, fuses the resulting landmark observations with IMU and GPS measurements into a joint maximum a posterior (MAP) estimation problem over the robot trajectory and all landmark positions, solved incrementally via factor graph optimization. A deferred data-association strategy bridges the two stages, ensuring that only filtered, outlier-free observations are committed to the graph.

Let $\mathcal{X} = \{\mathbf{T}_k, \mathbf{v}_k\}_{k=0}^K$ denote the robot trajectory states and $\mathcal{L} = \{\ell_j\}_{j=1}^J$ the landmark map. The complete estimation problem seeks the joint MAP estimate

$$\mathcal{X}^*, \mathcal{L}^* = \arg \max_{\mathcal{X}, \mathcal{L}} p(\mathcal{X}, \mathcal{L} | \mathcal{Z}) \quad (1)$$

where \mathcal{Z} aggregates all sensor measurements. Under the standard assumption of Gaussian noise and conditional independence given the variables each factor connects.

B. Segmentation and Tracking Dataset

Trunks and poles segmentation requires sufficient data to train neural network models. Unfortunately, those classes are not commonly included in public computer vision datasets. Hence, a significant data collection on the field has been carried out to perform the study. A new dataset has been gathered using an Intel Realsense D435 camera with resolution 640×480 pixels, mounted frontally on a ClearPath Husky rover. To promote multi-season generalization of the segmentation model, multiple data collection campaigns have been performed over the course of the entire year, capturing the vineyard across distinct phenological stages, from February to September, to account for significant variations in foliage density, grass growth, and illumination. The images have been manually labeled with ground truth masks, totally comprising 1600 RGB-D images. Moreover, a ground truth has been generated for tracking the instances of poles and trunks. For each frame of the video stream, a coherent ID

¹<https://github.com/PIC4SeR/VinePT-Map>



Fig. 2. VinePT-Map: a schematic pipeline of the semantic mapping framework for persistent landmarks in vineyards.

has been assigned to each instance to precisely validate the performance of the perception pipeline along the entire experiment duration.

C. Perception Front-End

The perception front-end receives time-synchronized colour images $\mathbf{I}_t \in \mathbb{R}^{H \times W \times 3}$ and aligned depth maps $\mathbf{D}_t \in \mathbb{R}^{H \times W}$ acquired by an RGB-D camera at each discrete time step t . Its output is a set of per-frame landmark descriptors:

$$\mathcal{O}_t = \{(\mathbf{p}_i^c, s_i, c_i, \tau_i)\}_{i=1}^{N_t}$$

where $\mathbf{p}_i^c \in \mathbb{R}^3$ is the estimated centroid in the camera frame, $s_i \in [0, 1]$ is the detection confidence, $c_i \in \{0, 1\}$ is the semantic class label (trunk or pole), and $\tau_i \in \mathbb{Z}$ is the persistent tracking identity assigned by the multi-object tracker. The processing chain is detailed in the following subsections.

Instance Segmentation and Tracking: The perception front-end employs a *YOLOv8-seg* architecture [22] for real-time segmentation. The model was fine-tuned on the custom multi-temporal vineyard dataset collected.

The dataset is partitioned into a training set (75%), a validation set (10%) and a testing set (15%) to ensure an unbiased performance evaluation. For each input frame \mathbf{I}_t , the model extracts two classes: trunks ($c = 0$) and poles ($c = 1$). Each detection \mathbf{d}_i is defined by a binary mask \mathbf{M}_i , a class prediction c_i , and a confidence score s_i . To ensure high precision, we discard detections where:

$$s_i < \theta_{\text{conf}} \quad \text{or} \quad c_i \notin \mathcal{C}_{\text{allowed}} \quad (2)$$

where $\theta_{\text{conf}} = 0.8$ is the minimum confidence threshold used and $\mathcal{C}_{\text{allowed}}$ is the set of permitted class identifiers. Finally, Non-Maximum Suppression is applied using an Intersection-over-Union (IoU) threshold θ_{IoU} to eliminate redundant predictions.

In order to ensure landmark ID temporal consistency across the image sequence, the segmentation output is integrated with the BoT-SORT [26] multi-object tracking framework. The purpose of this module is to enable the transition between individual frame detections and persistent landmark identification in image frames. To each valid detection is

assigned a unique, persistent integer track identity, denoted by the symbol τ_i . This identifier is the cornerstone of the system’s data-association mechanism. By treating all observations with the same value of the variable τ_i as a single physical entity, the system eliminates the computational overhead of visual re-identification in subsequent mapping and optimization stages.

Landmark Projection in 2D map: For each retained detection i with binary mask \mathbf{M}_i , the corresponding region in the aligned depth map \mathbf{D}_t is extracted, and the masked depth pixels are back-projected into a three-dimensional point cloud in the camera coordinate frame $\{C\}$. The back-projection follows the pinhole camera model. A validity filter rejects pixels whose depth values fall outside the admissible range $[z_{\min}, z_{\max}]$ or are non-finite. Masks yielding fewer than N_{\min} valid three-dimensional points are discarded to suppress detections originating from distant or poorly resolved objects. The resulting per-instance point cloud is denoted $\mathcal{P}_i = \{\mathbf{p}_n^c\}_{n=1}^{M_i} \subset \mathbb{R}^3$.

Landmark reference point computation: The reference position of each detected object is estimated from its reconstructed point cloud \mathcal{P}_i . The landmark spatial coordinates are derived through a localized centroid estimation that focuses exclusively on the lower segment of the detected object. By prioritizing this structurally rigid region, the system mitigates the impact of transient environmental noise, thereby facilitating more reliable data association and drift reduction within the subsequent mapping framework.

The isolation of the structurally stable base is implemented by sorting the landmark point cloud \mathcal{P}_i along the vertical camera axis (y -axis, oriented downward). To define the base subset \mathcal{P}_i^b , a trimming operation is applied whereby only the lowest fraction, specifically the first quarter, of the vertical distribution is retained. The 3D coordinates of the landmark reference point are subsequently derived via a hybrid mean–median estimator, formulated to balance precision with robustness:

$$\bar{\mathbf{p}}_i^c = [\text{mean}(\mathcal{P}_{i,x}^b), \text{mean}(\mathcal{P}_{i,y}^b), \text{median}(\mathcal{P}_{i,z}^b)]^\top \quad (3)$$

The lateral coordinates (x, y) are derived via the arithmetic mean, a choice that is substantiated by the relatively low noise levels in the lateral image plane. In contrast, the

depth coordinate (z) is determined using a median estimator. This provides critical resilience against heavy-tailed noise distributions and depth discontinuities that characterize depth measurement from RGB-D cameras in outdoor scenarios. The decoupling of the coordinate estimation in this way enables the system to achieve the statistical robustness required for unstructured environments while maintaining a lightweight computation profile.

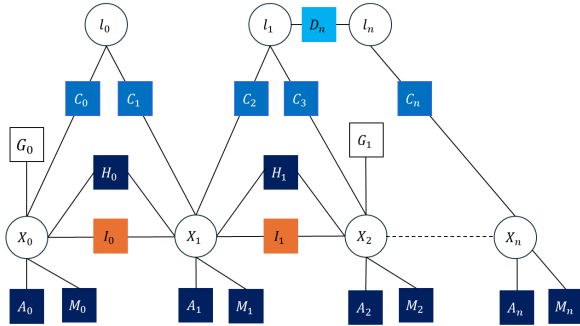


Fig. 3. VinePT-Map Factor Graph for poles and trunks mapping.

D. Localization and Mapping with Factor Graph

The back-end fuses landmark observations from the perception front-end III-C with inertial and GNSS measurements to jointly estimate the robot trajectory and a geo-referenced landmark map. The estimation is cast as MAP inference on a factor graph $\mathcal{G} = (\mathcal{V}, \mathcal{F})$, where \mathcal{V} denotes variable nodes and \mathcal{F} the set of factor (constraint) nodes, and is solved incrementally with the iSAM2 algorithm [27]. Fig. 3 illustrates the factor graph structure. Section III-D.1 presents the robot localisation formulation; Section III-D.2 describes the data-association strategy; Section III-D.3 details landmark mapping and post-hoc map refinement.

1) *Robot Localization*: At each keyframe $k = 0, \dots, K$ the robot state comprises its six-degree-of-freedom pose $\mathbf{T}_k \in SE(3)$, linear velocity $\mathbf{v}_k \in \mathbb{R}^3$. Graph construction is deferred until a valid GNSS fix and a calibrated AHRS orientation are simultaneously available. A set of factors constrains the robot’s state at each keyframe:

IMU Preintegration: Between consecutive keyframes, high-rate accelerometer and gyroscope readings are compressed into a single on-manifold pre-integrated measurement factor I_n following [28].

RTK-GPS Position: Each valid RTK-GPS fix constrains the translational component of the pose after conversion to ENU coordinates G_n .

Attitude: A two-dimensional factor A_n constrains roll and pitch by comparing the body-frame gravity projections of the estimated and AHRS-measured orientations, while leaving yaw unconstrained.

Magnetometer Heading: Absolute heading is maintained via a wrap-free parameterization. By formulating the residual of factor M_n using the rotation matrix columns, the system

avoids discontinuities at $\pm\pi$, ensuring smooth optimization gradients.

Non-Holonomic Constraints: To exploit the known kinematics of the rover, a soft factor H_n penalizes lateral and vertical velocities. A Huber robust cost is employed to maintain estimation integrity during maneuvers on slippery vineyard soil.

At each keyframe, the accumulated factors are committed to the iSAM2 optimiser [27], which performs partial re-elimination of its Bayes-tree representation, achieving amortised constant-time updates.

2) *Landmark Data Association*: This step of the pipeline addresses landmark association. The tracker identity τ_i assigned during the perception stage provides the primary short-term correspondence. The proposed system addresses global landmarks association through two complementary stages: deferred commitment with statistical outlier rejection, and class-aware spatial merging.

Deferred Commitment: Rather than being inserted into the factor graph immediately landmarks observations are buffered per tracker identity. Each buffered record contains the associated robot pose key, the bearing–range measurement with its propagated noise model, the detection confidence, and an approximate world-frame position $\tilde{\ell} = \mathbf{T}_k \circ \mathbf{p}^b$. The landmark commitment is triggered when the landmark is determined to be outside the current sensor field of view.

Outlier Rejection: Prior to commitment to optimization, the buffered world-frame landmark estimates $\{\tilde{\ell}^{(n)}\}$ are filtered using the Median Absolute Deviation (MAD). Observations whose normalized deviation $z_n = \|\tilde{\ell}^{(n)} - \tilde{\ell}_{\text{med}}\| / (1.4826 \cdot \text{MAD})$ exceeds the threshold $\lambda_{\text{MAD}} = 1.5$ are discarded.

Class-Aware Spatial Merging: The initial landmark position is set to the component-wise median of the inlier set: $\ell_j^{(0)} = \text{median}(\{\tilde{\ell}^{(n)}\}_{n \in \text{inliers}})$. Before a new variable is inserted, a nearest-neighbour search is performed among existing landmarks of the same semantic class. If an existing landmark $\ell_{j'}$ satisfies $\|\ell_j^{(0)} - \ell_{j'}\| < d_{\text{merge}}$ the incoming observations are redirected to $\ell_{j'}$, resolving fragmented tracks caused by occlusion-induced breaks without introducing duplicate variables. Restricting the search to same-class landmarks prevents spurious merges across semantically distinct object categories. d_{merge} holds two discrete values for each category: $0.5m$ for trunks and $1m$ for poles.

3) *Landmark Mapping*: In conclusion, the estimation of pole and trunk positions is achieved by the integration of landmark observations within the optimisation problem.

Bearing–Range Observation Model: Each committed observation, originally a Cartesian point \mathbf{p}^b in the body frame, is converted to a bearing $\mathbf{u} = \mathbf{p}^b / \|\mathbf{p}^b\| \in \mathbb{S}^2$ and range $r = \|\mathbf{p}^b\|$. The measurement covariance in bearing–range space is obtained by propagating the Cartesian sensor noise Σ_{xyz} through the transformation Jacobian:

$$\Sigma_{\text{BR}} = \mathbf{J} \Sigma_{xyz} \mathbf{J}^\top, \quad \mathbf{J} = \begin{bmatrix} \mathbf{B}^\top \frac{1}{r} (\mathbf{I}_3 - \mathbf{u}\mathbf{u}^\top) \\ \mathbf{u}^\top \end{bmatrix}$$

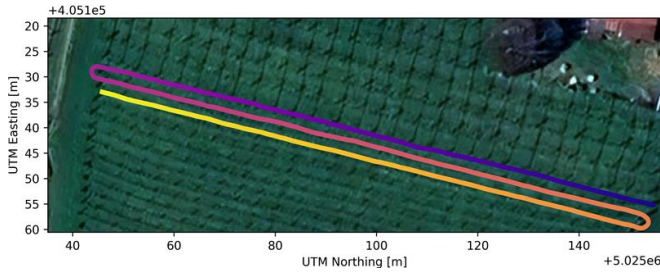


Fig. 4. Aerial view of the vineyard with the trajectory of the robot over three rows (starting from dark line, ending in yellow line), used to compute the incremental result of Table III.

where $\hat{\mathbf{u}}$ and \hat{r} are the predicted bearing and range, and $\mathbf{B}(\hat{\mathbf{u}}) \in \mathbb{R}^{3 \times 2}$ is an orthonormal basis spanning the tangent plane at $\hat{\mathbf{u}}$ on \mathbb{S}^2 . The resulting covariance is symmetrized and regularized to guarantee positive definiteness.

Map Refinement: Upon completion of the traverse, a consolidation step addresses residual landmark map fragmentation. Landmark positions are clustered per semantic class using DBSCAN with neighbourhood radius $\epsilon_{\text{cluster}}$. The $\epsilon_{\text{cluster}}$ is computed as one-half of the mean distance between objects of the same class that have been mapped. For each pair (ℓ_a, ℓ_b) within a cluster, a zero-displacement between-factor D_n is added. These soft constraints attract co-located landmarks toward a consensus position without irreversibly discarding variables. The complete graph is then re-optimized, yielding the final landmark map $\{\ell_j^*\}$ and robot trajectory $\{\mathbf{T}_k^*\}$ in the ENU frame, each landmark annotated with its semantic class $c_j \in \{\text{trunk}, \text{pole}\}$.

TABLE I
OVERVIEW OF FIELD CAMPAIGNS IN THE VINEYARDS.

Campaign	Weather	Plant Growth	Grass Height
12/02	Cloudy	Stem, no leaves	Low (~ 5 cm)
20/03	Sunny	Stem, no leaves	Medium (~ 20 cm)
14/08	Sunny	Branches, leaves, fruit	Low (~ 5 cm)
11/09	Cloudy	Branches, leaves, fruit	Medium (~ 20 cm)

IV. EXPERIMENTS

Four field campaigns have been carried out to collect the data and trajectories of the robot in different seasons. Table I reports the field and weather conditions of each campaign, affecting the performance of perception and SLAM systems. The experiments has been performed with a Husky A200 rover from ClearPath Robotics (size 990 x 670 x 390 mm) mounting an on-board computer with an Intel i7-6700E processor, 16 GB DDR4 RAM. The adopted sensor suite includes an RGB-D Intel Realsense D435 camera, providing aligned RGB and depth images, an accurate AHRS MicroS-train 3DM-GX5, and a RTK-GPS.

The rover has been teleoperated with $v_{max} = 1$ m/s and $\omega_{max} = 2.0$ rad/s following the desired trajectory along three consecutive rows of the vineyard, about 100 m long, shown in Fig 4. In some trajectory segments, the difficulty of remote driving, the terrain irregularity, and the

TABLE II
RESULTS OF LANDMARKS INSTANCE SEGMENTATION AND TRACKING.
THE BEST SEASONAL RESULTS ARE HIGHLIGHTED IN BOLD.

Class	Date	Box mAP50	Mask mAP50	HOTA	AssA
Trunks	02-12	0.934	0.928	89.1	90.3
	03-20	0.961	0.946	85.4	89.8
	08-14	0.91	0.916	74.7	87.1
	09-11	0.863	0.859	81.3	84.8
	Overall	0.914	0.908	82.6	88.0
Poles	02-12	0.878	0.833	72.4	74.7
	03-20	0.895	0.823	70.8	72.5
	08-14	0.913	0.902	51.7	95.1
	09-11	0.828	0.855	67.6	74.9
	Overall	0.887	0.844	65.6	79.3

TABLE III
QUANTITATIVE EVALUATION OF POLES LANDMARKS MAPPING USING
GEOREFERENCED POSITIONS AS GROUND TRUTH. THE METRICS ARE
REPORTED INCREMENTALLY OVER THREE CONSECUTIVE ROWS.

N. Rows	1		2		3	
Date	MAE [m]↓	TP(%)↑	MAE [m]↓	TP(%)↑	MAE [m]↓	TP(%)↑
02-11	0.20	100.0	0.18	97.3	0.18	97.1
03-20	0.24	96.2	0.22	96.3	0.27	91.1
08-14	0.25	98.1	0.24	97.2	0.24	93.1
09-11	0.31	100	0.29	96.3	0.26	97.2

small obstacles led to sudden drifts of the rover, missing some landmarks with the camera on one side. This behavior can also occur in realistic autonomous driving settings. The ground truth position of the pole landmarks on the field has been obtained with an aerial georeferenced image.

V. RESULTS

In this section, the resulting effectiveness of the VinePT-Map system has been evaluated on both perception and mapping aspects. First, we measured the reliability of the detection and tracking pipeline on our custom image dataset spanning all the seasons, to evaluate how well it identifies and tracks poles and trunks. Hence, the generalization of the detection model over the different conditions has been analyzed. Then, the spatial accuracy of the semantic maps obtained through the factor graph optimization is discussed under different phenological vegetation stages.

A. Visual Perception Evaluation

A major challenge for agricultural robots is maintaining a reliable perception of relevant features, even when the environment changes drastically throughout the year. We evaluated our perception pipeline using three metrics: Mean Average Precision (mAP50), Higher Order Tracking Accuracy (HOTA) and Association Accuracy (AssA). As shown in Table II, the system performed consistently across all temporal evaluations.

Detection: During the winter and early spring (February and March), when the vines were bare stems, trunk detection was most effective, achieving Box mAP50 scores of 0.934 and 0.961, respectively. Importantly, as the canopy

transitioned to the full foliage and fruiting stages in August and September, the framework maintained high detection rates, achieving Box mAP50 scores of 0.910 and 0.863, respectively. This marginal variance empirically confirms that detection can perform consistently throughout each stage of phenological growth. Detection and segmentation performances have not shown performance degradation even in more complex seasons such as summer and autumn, when foliage introduces more noise and covers part of the poles and trunks. In addition, our solution has proven robustness also to different lighting conditions due to the weather and light direction.

Tracking: Persistent tracking is paramount to mitigate the perceptual aliasing inherent in repetitive crop rows. The system yielded an overall AssA of 88.0 for trunks and 79.3 for poles. Notably, the pole tracking module achieved an exceptional AssA peak of 95.1% during the complex summer traverse in August, demonstrating the tracker’s ability to maintain consistent tracking IDs despite the dense vegetation and changing lighting conditions. The overall results of tracking can be partly attributed to the great performance of the detection algorithm. In fact, stable detections over time pave the way for a more stable functioning of the tracking algorithm. Moreover, due to the limited movements of the tracked object, the tracker is able to provide more robust results.

Inference: The real-time capability of the perception pipeline is fundamental to be deployed directly on the autonomous platform. Hence, the segmentation and tracking pipeline has been tested for a real test on the robot computational hardware. On the i7-6700E processor of the robot board, using an image resolution of 640×480 px, the segmentation model and tracking pipeline can run at 30 Hz, which is the acquisition frequency of the camera.

B. Mapping Evaluation

A quantitative evaluation of the performance of the VinePT-Map semantic framework is proposed here. The geometrical accuracy of the generated poles landmarks maps is directly computed. We compare the computed maps, optimized by the factor-graph methodology, against georeferenced ground truth data acquired through precise aerial images and photogrammetry software. The adopted metrics are the Mean Absolute Error (MAE) to directly compare the estimate with the ground truth value, and the percentage of landmarks mapped correctly. The results are reported in Table III.

The mapping pipeline demonstrated high precision, particularly during the winter campaign in February, when optimal visibility is achieved without foliage. It recorded a MAE of 0.18 m when mapping two or three consecutive rows. In August, with the most challenging conditions of both grass and canopies, the maximum error marginally increased to only 0.32 m. This result confirms our hypothesis that poles and skeletal elements of the field remain visible; thus, they represent persistent landmarks. Moreover, the depth-sensor noise induced by thick vegetation’s occlusions can

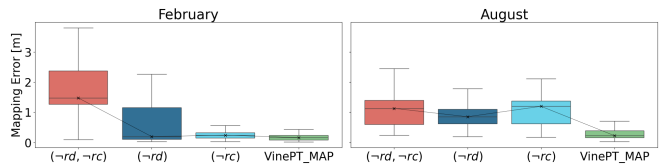


Fig. 5. Box plots of the ablation study results on poles mapping error. The relevance of the landmark reference point computation method (rd) and the data association method (rc) is highlighted by excluding them from the pipeline.

be effectively bounded by the factor graph’s robust geometrical constraints. The percentage of True Positive (TP)% in Table III evaluates the number of poles landmarks correctly mapped and re-associated over multiple observations. The system’s ability to persistently capture the topology of the vineyard is reflected in its high landmark mapping rates. During the winter and summer surveys, the percentage of successfully mapped poles consistently exceeded 93.1%, reaching 100% in the primary row in February.

C. Ablation study

An ablation study is performed to investigate the impact of fundamental perception steps on the mapping results. The box plots of poles mapping error over three consecutive vineyard rows, for the field campaign of February and August, are reported in Fig.5. The performance of the VinePT-Map system is analyzed, removing the landmark reference point computation method (rd) and the deferred commitment with MAD-based outlier rejection (rc), explained in Section III. In February, with leafless canopies and structural elements fully exposed, the results clearly demonstrate the positive impact of each component alone. In this scenario, both contributions independently yield substantial improvements in mapping accuracy, reducing the median error from 1.4 m in the baseline configuration $(-rc, -rd)$ to 0.16 m in the full VinePT-Map pipeline. In these field conditions, the robust reference-point extraction method (rd) significantly contributes to achieving accuracy comparable to the complete system. However, under the more challenging conditions of August, with thick canopies and fruits obstructing the measurement process, the same trend does not hold. Under these adverse conditions, neither component acting independently is sufficient to produce a meaningful improvement over the baseline: the median error and variance of the mapping error remain elevated across both partial configurations $(-rc)$ and $(-rd)$. Only the full VinePT-Map pipeline, integrating both contributions, achieves a median error of 0.22 m. These ablation results provide empirical evidence that the two proposed components are jointly necessary to ensure robust and consistent landmark mapping performance across the full range of seasonal conditions encountered in real-world vineyard environments.

D. Qualitative Map Evaluation

The semantic maps of poles, landmarks, and associated ground truth are shown in Fig. 6. The zoom-in view also

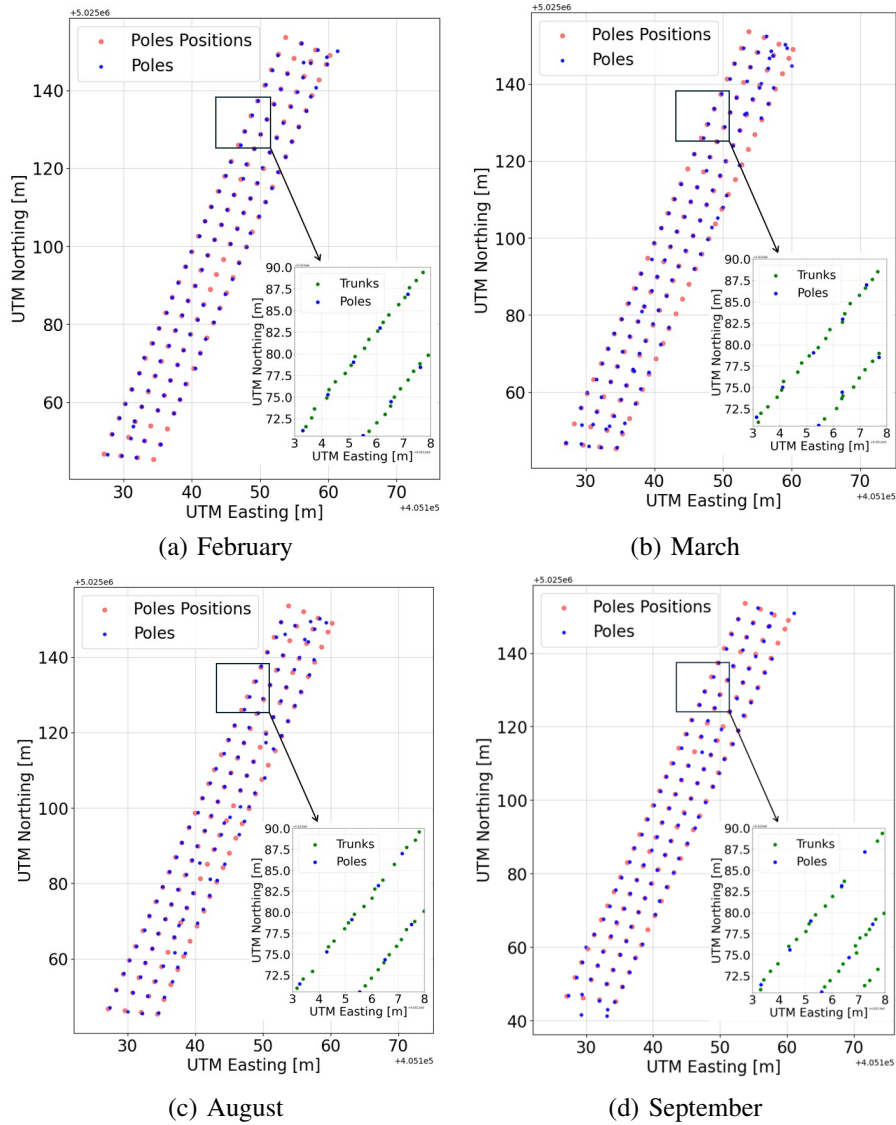


Fig. 6. Map of vineyard poles and trunks over three consecutive rows in February, March, August, and September, with a zoomed-in view of the poles and trunks.

shows the trunk’s position estimated for a certain portion of the trajectory. In general, the highest uncertainty in landmarks mapping is localized at the end of the rows, where the rover performs a strict turn, losing some poles, and plants may present irregular dispositions. In February, a series of poles in the central part of the map, second row, were removed for substitution and have not been mapped by the robot. In March, the map was correctly updated. On the other hand, some poles have been missed on the third row (March) due to abrupt heading changes and oscillations of the robot. August presents the most frequent re-association and precision errors, being the most challenging scenarios with thick canopies and grapes.

VI. CONCLUSIONS

This work presented VinePT-Map, a semantic mapping framework for vineyards that leverages persistent structural landmarks to enable robust and season-agnostic localization

of autonomous robots. By formulating the problem within a factor graph framework and fusing robot localization and RGB-D measurements through structural geometric constraints, the proposed approach reduces susceptibility to perceptual aliasing and environmental variability.

The integration of an efficient instance segmentation and tracking pipeline, coupled with a clustering-based refinement strategy, allows reliable landmark detection using low-cost sensors and onboard computation, supporting practical field deployment. Extensive multi-season experiments, together with the introduction of a dedicated dataset for poles and trunks, validate the robustness of both perception and mapping components under varying illumination, canopy density, and weather conditions.

Overall, the results demonstrate that semantic vineyard maps based on permanent skeletal infrastructure can be obtained with high precision in different seasons and field conditions, providing a stable spatial foundation for long-

term autonomous operation. The ablation study remarked the importance of a robust perception pipeline to obtain reliable field maps. Future work will be focused on the extension of the experimentation to vineyards of different types, collecting also the georeferenced ground truth of trunk landmarks. A pivotal step will be the integration of the semantic map obtained into a landmark-based localization system, comparing the performance with GPS localization and exploring the reliability of low-cost visual solutions. Moreover, the semantic skeletal map, target of this study, constitutes a first ground layer of a broader semantic field description to be build on top, comprising fruits poses and features that will be the main focus of agricultural robots activity.

REFERENCES

- [1] Z. Zhai, J. F. Martínez, V. Beltran, and N. L. Martínez, “Decision support systems for agriculture 4.0: Survey and challenges,” *Computers and Electronics in Agriculture*, vol. 170, p. 105256, 2020.
- [2] S. Cerrato, V. Mazzia, F. Salvetti, M. Martini, S. Angarano, A. Navone, and M. Chiaberge, “A deep learning driven algorithmic pipeline for autonomous navigation in row-based crops,” *IEEE Access*, 2024.
- [3] M. Martini, A. Eirale, B. Tuberga, M. Ambrosio, A. Ostuni, F. Messina, L. Mazzara, and M. Chiaberge, “Enhancing navigation benchmarking and perception data generation for row-based crops in simulation,” in *Precision agriculture’23*. Wageningen Academic, 2023, pp. 451–457.
- [4] D. Bigelow and A. Borchers, “Major uses of land in the united states, 2012,” *Economic Information Bulletin Number 178*, no. 1476-2017-4340, p. 69, 2017.
- [5] W. Winterhalter, F. Fleckenstein, C. Dornhege, and W. Burgard, “Localization for precision navigation in agricultural fields—beyond crop row following,” *Journal of Field Robotics*, vol. 38, no. 3, pp. 429–451, 2021.
- [6] Z. Diao, L. Chen, Y. Yang, Y. Liu, J. Yan, S. He, and B. Zhang, “Localization technologies for smart agriculture and precision farming: A review,” *Computers and Electronics in Agriculture*, vol. 236, p. 110464, 2025.
- [7] F. Salvetti, S. Angarano, M. Martini, S. Cerrato, and M. Chiaberge, “Waypoint generation in row-based crops with deep learning and contrastive clustering,” in *Machine Learning and Knowledge Discovery in Databases: European Conference, ECML PKDD 2022, Grenoble, France, September 19–23, 2022, Proceedings, Part VI*. Springer, 2023, pp. 203–218.
- [8] H. Wu, X. Wang, X. Chen, Y. Zhang, and Y. Zhang, “Review on key technologies for autonomous navigation in field agricultural machinery,” *Agriculture*, vol. 15, no. 12, p. 1297, 2025.
- [9] W. Hua, Z. Zhang, W. Zhang, X. Liu, C. Hu, Y. He, M. Mhamed, X. Li, H. Dong, C. K. Saha *et al.*, “Key technologies in apple harvesting robot for standardized orchards: A comprehensive review of innovations, challenges, and future directions,” *Computers and Electronics in Agriculture*, vol. 235, p. 110343, 2025.
- [10] L. Droukas, Z. Doulgeri, N. L. Tsakiridis, D. Triantafyllou, I. Kleitsiotis, I. Mariolis, D. Giakoumis, D. Tzovaras, D. Kateris, and D. Bochtis, “A survey of robotic harvesting systems and enabling technologies,” *Journal of Intelligent & Robotic Systems*, vol. 107, no. 2, p. 21, 2023.
- [11] A. Feng, J. Zhou, E. D. Vories, K. A. Sudduth, and M. Zhang, “Yield estimation in cotton using uav-based multi-sensor imagery,” *Biosystems Engineering*, vol. 193, pp. 101–114, 2020.
- [12] M. S. U. Khan, T. Ahmed, and H. Chen, “A review of slam techniques for agricultural robotics: Challenges, architectures, and future directions,” in *2025 IEEE 15th International Conference on CYBER Technology in Automation, Control, and Intelligent Systems (CYBER)*, 2025, pp. 598–603.
- [13] S. Singh, R. Vaishnav, S. Gautam, and S. Banerjee, “Agricultural robotics: A comprehensive review of applications, challenges and future prospects,” in *2024 2nd International Conference on Artificial Intelligence and Machine Learning Applications Theme: Healthcare and Internet of Things (AIMLA)*, 2024, pp. 1–8.
- [14] C. Lehnert, D. Tsai, A. Eriksson, and C. McCool, “3d move to see: Multi-perspective visual servoing towards the next best view within unstructured and occluded environments,” in *2019 IEEE/RSJ International Conference on Intelligent Robots and Systems (IROS)*, 2019, pp. 3890–3897.
- [15] H. Ding, B. Zhang, J. Zhou, Y. Yan, G. Tian, and B. Gu, “Recent developments and applications of simultaneous localization and mapping in agriculture,” *Journal of Field Robotics*, vol. 39, no. 6, pp. 956–983, 2022. [Online]. Available: <https://onlinelibrary.wiley.com/doi/abs/10.1002/rob.22077>
- [16] Y. Wang, W. Jia, M. Ou, X. Wang, and X. Dong, “A review of orchard canopy perception technologies for variable-rate spraying,” *Sensors*, vol. 25, no. 16, 2025. [Online]. Available: <https://www.mdpi.com/1424-8220/25/16/4898>
- [17] S. Pan, Y. Hu, A. Ohya, and A. Yorozu, “Robust localization for agricultural robots in seasonally changing orchards using edge-based lidar segmentation and imu fusion,” in *2025 13th International Conference on Control, Mechatronics and Automation (ICMA)*, 2025, pp. 135–141.
- [18] R. de Silva, J. Cox, J. R. Heselden, M. Popovic, C. Cadena, and R. Polvara, “Semantic-aware particle filter for reliable vineyard robot localisation,” 2025. [Online]. Available: <https://arxiv.org/abs/2509.18342>
- [19] A. S. Aguiar, F. Neves dos Santos, H. Sobreira, J. Boaventura-Cunha, and A. J. Sousa, “Localization and mapping on agriculture based on point-feature extraction and semiplanes segmentation from 3d lidar data,” *Frontiers in Robotics and AI*, vol. Volume 9 - 2022, 2022. [Online]. Available: <https://www.frontiersin.org/journals/robotics-and-ai/articles/10.3389/frobt.2022.832165>
- [20] R. A. Epstein, E. Z. Patai, J. B. Julian, and H. J. Spiers, “The cognitive map in humans: spatial navigation and beyond,” *Nature Neuroscience*, vol. 20, no. 11, pp. 1504–1513, Nov 2017. [Online]. Available: <https://doi.org/10.1038/nn.4656>
- [21] D. Rapado-Rincon and G. Kootstra, “Tree-slam: semantic object slam for efficient mapping of individual trees in orchards,” *Smart Agricultural Technology*, p. 101439, 2025.
- [22] J. Redmon, S. Divvala, R. Girshick, and A. Farhadi, “You Only Look Once: Unified, Real-Time Object Detection,” in *2016 IEEE Conference on Computer Vision and Pattern Recognition (CVPR)*. IEEE, pp. 779–788. [Online]. Available: <http://ieeexplore.ieee.org/document/7780460/>
- [23] H. Moreno, C. Valero, J. M. Bengochea-Guevara, Á. Ribeiro, M. Garrido-Izard, and D. Andújar, “On-ground vineyard reconstruction using a LiDAR-based automated system,” *Sensors (Basel)*, vol. 20, no. 4, p. 1102, Feb. 2020.
- [24] A. S. Aguiar, F. N. Dos Santos, J. B. Cunha, H. Sobreira, and A. J. Sousa, “Localization and mapping for robots in agriculture and forestry: A survey,” *Robotics*, vol. 9, no. 4, p. 97, 2020.
- [25] S. Jiang, P. Qi, L. Han, L. Liu, Y. Li, Z. Huang, Y. Liu, and X. He, “Navigation system for orchard spraying robot based on 3d lidar slam with ndt_lcp point cloud registration,” *Computers and Electronics in Agriculture*, vol. 220, p. 108870, 2024. [Online]. Available: <https://www.sciencedirect.com/science/article/pii/S0168169924002618>
- [26] N. Aharon, R. Orfaig, and B.-Z. Bobrovsky, “Bot-sort: Robust associations multi-pedestrian tracking,” 2022. [Online]. Available: <https://arxiv.org/abs/2206.14651>
- [27] M. Kaess, H. Johannsson, R. Roberts, V. Ila, J. Leonard, and F. Dellaert, “isam2: Incremental smoothing and mapping with fluid relinearization and incremental variable reordering,” in *2011 IEEE International Conference on Robotics and Automation*, 2011, pp. 3281–3288.
- [28] C. Forster, L. Carlone, F. Dellaert, and D. Scaramuzza, “On-manifold preintegration for real-time visual–inertial odometry,” *IEEE Transactions on Robotics*, vol. 33, no. 1, pp. 1–21, 2017.